

On-Chip Rayleigh Imaging and Spectroscopy of Carbon Nanotubes

Daniel Y. Joh,^{†,‡} Lihong H. Herman,[†] Sang-Yong Ju,[‡] Jesse Kinder,[‡] Michael A. Segal,[‡] Jeffrey N. Johnson,[‡] Garnet K. L. Chan,[‡] and Jiwoong Park^{*,‡,§}

[†]School of Applied and Engineering Physics, [‡]Department of Chemistry and Chemical Biology, and [§]Kavli Institute at Cornell for Nanoscale Science, Cornell University, Ithaca, New York 14853

ABSTRACT We report a novel on-chip Rayleigh imaging technique using wide-field laser illumination to measure optical scattering from individual single-walled carbon nanotubes (SWNTs) on a solid substrate with high spatial and spectral resolution. This method in conjunction with calibrated AFM measurements accurately measures the resonance energies and diameters for a large number of SWNTs in parallel. We apply this technique for fast mapping of key SWNT parameters, including the electronic-types and chiral indices for individual SWNTs, position and frequency of chirality-changing events, and intertube interactions in both bundled and distant SWNTs.

KEYWORDS Carbon nanotubes, Rayleigh scattering, optical properties, electronic structure, heterojunctions, intertube coupling

Carbon nanotubes are a heterogeneous group of materials. As-grown carbon nanotubes can comprise single-walled carbon nanotubes (SWNTs) with a wide range of structural (n, m) indices, multiwalled carbon nanotubes (MWNTs), nanotube bundles, and SWNTs that change chirality due to structural defects. Furthermore, their interactions with the environment and other neighboring nanotubes directly affect their electronic and optical properties.^{1–6} Transmission electron microscopy,⁷ scanning tunneling microscopy,^{8–10} and various optical spectroscopic techniques have been used to characterize individual carbon nanotubes.^{2,11–18} However, these methods usually require long data acquisition times and/or complicated sample preparation, which limits their use as a general characterization method for SWNTs. An ideal characterization method would require little sample preparation, minimize potential damage to SWNTs, and allow the characterized SWNTs to be used for subsequent experiments or device fabrication. Optical imaging of carbon nanotubes placed directly on a solid substrate meets these requirements and allows rapid visualization and spectral resolution of individual nanotubes with relative ease.

The optical properties of SWNTs originate from their 1D electron band structure. Within a noninteracting single-particle picture, the density of states for SWNTs has sharp resonance peaks called van Hove singularities¹⁹ (vHs) (Figure 1d). Electron–electron interactions modify this simple picture, leading to a significant increase in the energies of continuum states and the formation of strongly bound exciton states.²⁰ While electrical conductance of SWNTs is governed by the properties of the continuum states, optical

properties of SWNTs are determined by the structure of the excitonic states.¹¹ Much work has been done to understand the optical properties of SWNTs using Raman,^{2,14,17,18,21} photoluminescence,^{11,14,15} Rayleigh,^{3,12,13,22} and absorption spectroscopy^{16,23} to probe both ensembles and individual SWNTs. Resonances associated with the excitonic states and vHs have been the main focus of these studies, since they provide a direct measurement of interband transition energies for SWNTs (Figure 1d). By identifying the resonance energies, it is possible to determine the electrical property of an individual SWNT (metallic (M) or semiconducting (S)), and the chiral index, (n, m).

Compared to Raman and photoluminescence measurements, Rayleigh spectroscopy presents many advantages. It relies on elastic scattering (which is several orders of magnitude brighter than inelastic scattering), can be applied to both semiconducting and metallic nanotubes, and allows visible wavelength excitation and detection for better spatial resolution and detection sensitivity. In a series of recent papers, Heinz et al. reported Rayleigh scattering measurements from individual SWNTs and nanotube bundles and used this technique to determine chiral indices and study intertube coupling effects.^{3,12,13} In their studies, individual nanotubes were suspended over a fabricated gap and illuminated by a focused laser beam one at a time to avoid the intense scattering from the substrate itself. Although this method presents excellent signal-to-noise ratio, the suspended geometry limits its spatial resolution, diameter range of observed nanotubes (typically 1.5 nm or larger), and correlation with other measurements (such as AFM).

To overcome these problems, we developed a broadband laser-based darkfield microscope to minimize the background scattering without suspending the SWNTs, allowing Rayleigh imaging of SWNTs directly on a solid substrate for the first time (Figure 1a). To minimize the background

* To whom correspondence should be addressed. E-mail: jpark@cornell.edu.

Received for review: 04/9/2010

Published on Web: 00/00/0000



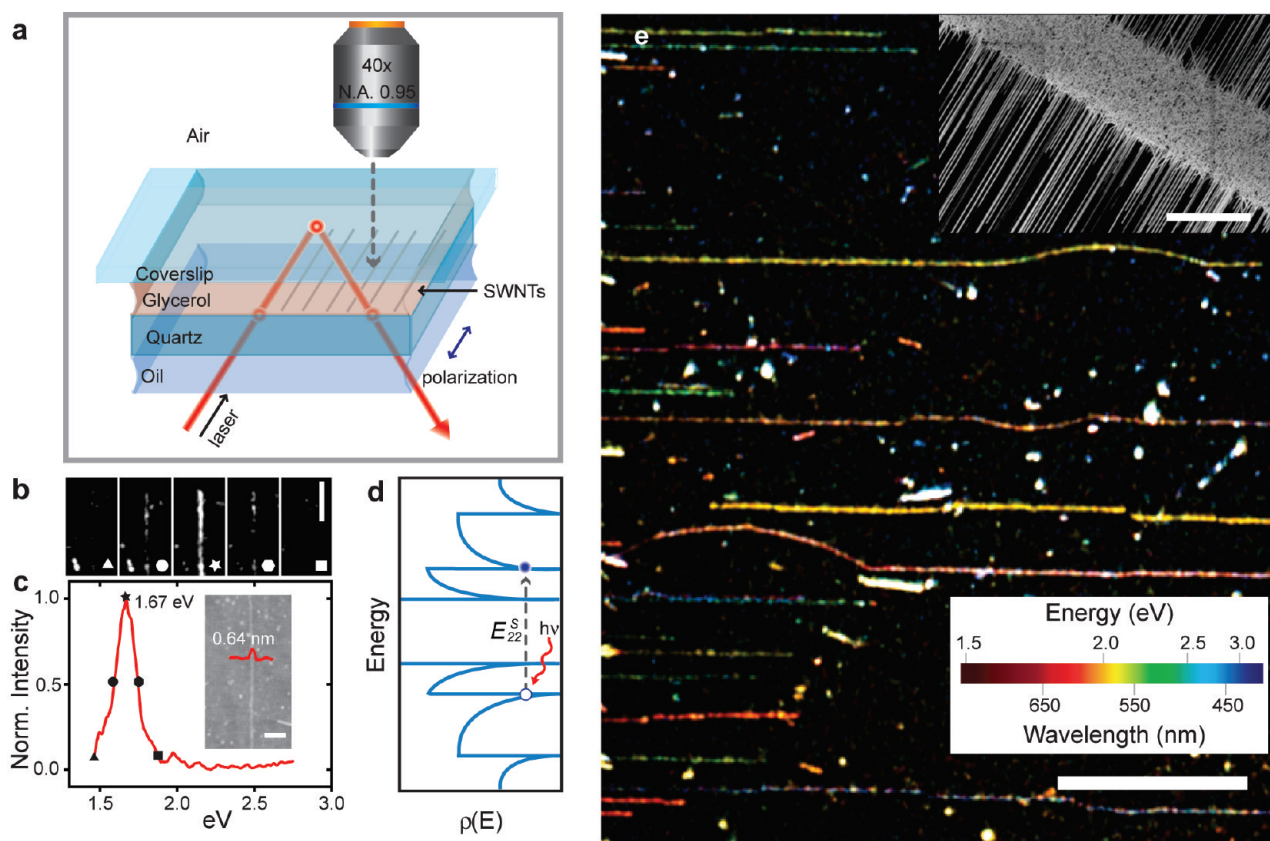


FIGURE 1. On-chip Rayleigh imaging of SWNTs. (a) Schematic of the optical setup. The incident laser is introduced at an angle, travels through a set of index-matched media, and is reflected completely at the uppermost interface with a lower refractive index medium (air). (b,c) Rayleigh scattering spectrum (c) of a SWNT ($d_{\text{AFM}} = 0.64$ nm) as a function of excitation energy and its corresponding spatial Rayleigh image snapshots (b) at different frequencies, indicated by symbols in (c). The spectrum in (c) and all subsequent spectra provided are normalized to the spectral peak. (d) Diagram depicting the density of states $\rho(E)$ and van Hove singularities for an $E_{22}^{\text{S}1}$ transition in a semiconducting SWNT. (e) Representative spatial Rayleigh image shows more than 20 SWNTs simultaneously (in false color corresponding to λ_{peak}). Scale bar, 20 μm . Inset: SEM image of a typical sample in a more dense area. Scale bar, 10 μm .

scattering, the substrate with SWNTs was coated with an index-matching medium of glycerol, whose refractive index (ca. 1.47) is similar to that of quartz (ca. 1.54). Moreover, the laser excitation geometry prevents incident light from entering the detection optics. A charge-coupled device (CCD) camera and a high numerical aperture (N.A.) objective lens were used to detect the elastically scattered photons from individual SWNTs under wide-field illumination on the substrate while the excitation wavelength λ of the excitation laser (Fianium Ltd., model SC450) was scanned from 450 to 850 nm with a spectral bandwidth of 20 nm. The sample used in this study was an array of highly aligned nanotubes directly grown on a quartz substrate with etched alignment marks using a chemical vapor deposition (CVD) method reported earlier,²⁴ and the typical nanotube diameter measured by AFM (d_{AFM}) ranges from 0.5 to 2.2 nm. The excitation laser was linearly polarized parallel to the nanotube axis, and all measurements were performed under ambient conditions (see Supporting Information for further details).

Our setup produces optical images of individual SWNTs with high signal-to-noise ratio. In Figure 1b, we show five

representative images out of a total of 200 frames (15 s integration time per frame) measured at different λ for a SWNT with $d_{\text{AFM}} = 0.64$ nm. The SWNT “blinks” in the middle frame marked by star. Tracing the light intensity from all 200 images from this SWNT, we observe a single resonance at 1.67 eV, as shown in Figure 1c. In this geometry, the vast majority of the detected photons are due to elastic (Rayleigh) scattering. This is confirmed by comparing darkfield images with and without a matching bandpass filter (bandwidth <10 nm) in the detection pathway, which would reject photons from Raman scattering and photoluminescence (see Supporting Information). Hence, the plot in Figure 1c is the Rayleigh spectrum of the SWNT imaged here, and the observed peak corresponds to a scattering resonance where the photon energy matches the energy of an allowed interband (excitonic) transition.

By obtaining Rayleigh spectra for each pixel of the widefield illuminated area (approximately $70 \times 80 \mu\text{m}^2$) from a single measurement run, we can generate a spatial map of key resonance parameters for each SWNT, including the resonance wavelength (λ_{peak}), intensity, and peak width. Figure 1e shows a color map of λ_{peak} in a region on the

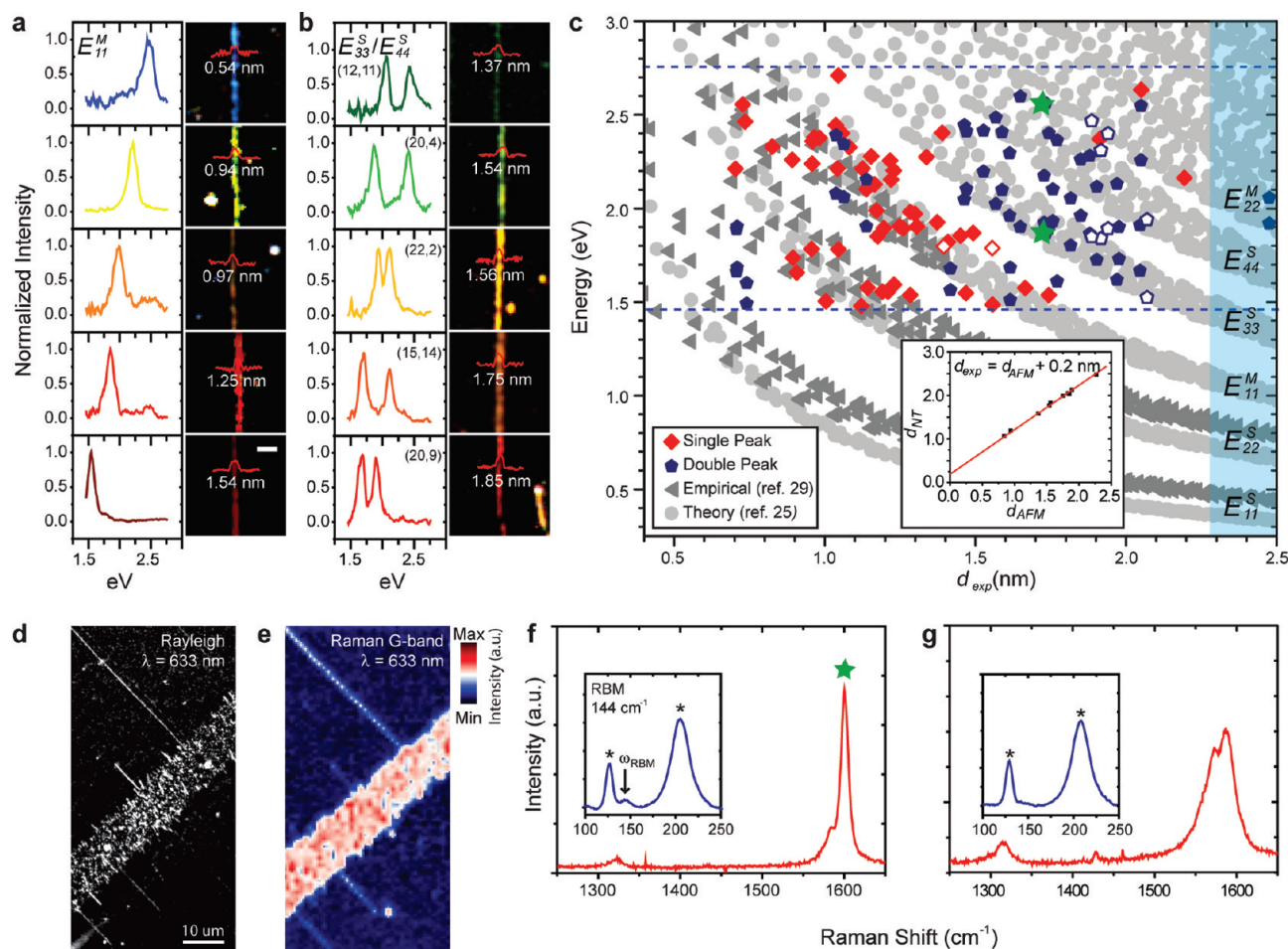


FIGURE 2. Electronic type assignments of SWNTs from Rayleigh imaging. (a, b) Color Rayleigh images of metallic (a) and semiconducting (b) SWNTs, along with their corresponding optical spectra and AFM height traces (shown in red). The resonant Rayleigh peaks in (a) correspond to E_{11}^M transitions and those in (b) to E_{33}^S/E_{44}^S transitions. Scale bar, 2 μm . (c) Experimental Kataura plot. SWNTs exhibiting either one peak (red) or two peaks (blue) from their Rayleigh spectra within our excitation energy range (blue dashed lines) are plotted using d_{exp} for the diameter axis ($d_{exp} = d_{AFM} + 0.2 \text{ nm}$). Theoretical tight-binding (light gray circles with $\gamma_0 = 2.9 \text{ eV}$) and published empirical data (dark gray triangles) are provided for comparison. Resonant Raman spectroscopy was performed on several individual SWNTs indicated by hollow data points. Inset: A correlation plot of d_{NT} vs d_{AFM} . (d) Black and white Rayleigh image taken at 633 nm. (e) Corresponding 2D confocal Raman image of the G-band intensity of the region shown in (d). (f) Representative Raman spectrum (excitation wavelength 633 nm) for the semiconducting^{17,7} SWNT labeled by green stars on the Kataura plot in Figure 2c. Quartz Raman peaks indicated by black asterisks. (g) Representative Raman spectrum for a metallic SWNT.

substrate that contains mostly SWNTs with the brightness of each spot corresponding to the scattering intensity. Since their scattering intensity depends strongly on the excitation wavelength, the SWNTs in this image exhibit distinct colors that are generally uniform throughout their length. In comparison, multiwalled carbon nanotubes show broadband scattering with much less wavelength dependence under the same measurement conditions (see Supporting Information). Comparing a typical color image and its corresponding AFM image confirms that all SWNTs (even as small as $d_{AFM} = 0.5 \text{ nm}$) are visible in our Rayleigh image (see Supporting Information). An SEM image of a more dense area of our sample is shown in the inset of Figure 1e.

The data shown in Figure 1 clearly demonstrate that our on-chip Rayleigh imaging scheme allows rapid and accurate measurement of the Rayleigh scattering spectra for a large

number of SWNTs with submicrometer spatial resolution. Below, we discuss the application of this technique to (1) determine chirality indices (n, m) and electronic types for SWNTs, (2) spatially resolve and measure the frequency of individual chirality changing events, and (3) study the intertube coupling effects as the distance between two SWNTs varies.

Spatially resolved Rayleigh imaging combined with calibrated AFM measurements provides a powerful method for identifying the electrical properties (M/S) and the chirality indices (n, m) for a large number of SWNTs with high throughput. In Figure 2a, we show five representative SWNTs showing a single peak in their Rayleigh spectra within our excitation range, and similar data is shown in Figure 2b for nanotubes with two peaks in their optical spectra. We also measured their AFM heights d_{AFM} (as shown by the red height

TABLE 1. Physical and Spectroscopic Data for Several SWNTs from AFM and Rayleigh Scattering Measurements^a

(n, m)	d_{AFM}	θ (°)	d_{NT}	transition	E_{ii}^{exp} (eV)	E_{ii}^{calc} (eV)	fwhm _{exp} (meV)
(12, 11)	1.37	28.6	1.58	E_{35}^S	2.50	2.06	87
				E_{44}^S	2.44	2.56	128
(20, 4)	1.54	8.9	1.77	E_{35}^S	1.87	1.78	106
				E_{44}^S	2.41	2.47	130
(22, 2)	1.56	4.3	1.83	E_{35}^S	1.93	1.91	92
				E_{44}^S	2.10	2.12	121
(15, 14)	1.75	28.9	1.99	E_{35}^S	1.70	1.65	132
				E_{44}^S	2.11	2.06	83
(20, 9)	1.85	17.7	2.04	E_{35}^S	1.67	1.66	100
				E_{44}^S	1.91	1.94	81
(16, 15)	1.89	28.9	2.13	E_{35}^S	1.52	1.54	92
				E_{44}^S	1.92	1.93	62
(13, 1)	0.84	3.7	1.07	$E_{11}^M(-)$	2.08	2.16	196
				$E_{11}^M(+)$	2.39	2.46	105
(15, 0)	0.94	0	1.19	$E_{11}^M(-)$	1.90	1.96	149
				$E_{11}^M(+)$	2.15	2.22	67
(23, 5)	1.83	9.6	2.05	$E_{11}^M(-)$	2.23	2.26	75
				$E_{11}^M(+)$	2.52	2.55	110
(25, 10)	2.27	16.1	2.48	$E_{11}^M(-)$	1.88	1.92	82
				$E_{11}^M(+)$	1.99	2.06	102

^a SWNTs are identified by their chiral indices (n, m) and their corresponding true diameter (d_{NT}) and chiral angle θ . The experimentally determined electronic transitions are denoted by E_{ii}^{exp} , and those predicted by ref 25 (E_{ii}^{calc}). The higher and lower energy peaks for metallic nanotube transitions are denoted by $E_{ii}^M(+)$ and $E_{ii}^M(-)$, respectively. The experimental peak widths (fwhm_{exp}) are also provided, which were deconvolved from the raw peak widths (fwhm_{raw}) after considering the 20 nm bandwidth of the exciting laser (BW_{probe}) using the relationship $\text{fwhm}_{\text{exp}} = (\text{fwhm}_{\text{raw}}^2 - \text{BW}_{\text{probe}}^2)^{1/2}$.

traces in the Rayleigh images) after carefully removing the glycerol. For the nanotubes shown in Figure 2a, the interband transition energy decreases with increasing d_{AFM} . Likewise, the average of the two resonance energies for the nanotubes in Figure 2b also decreases with increasing d_{AFM} , even though the individual peaks do not follow this trend. In fact, the optical spectra of SWNTs are expected to behave in this manner; the data in Figure 2a matches the expected behavior of metallic SWNTs whereas the data shown in Figure 2b corresponds to that of semiconducting tubes.^{19,25}

In Table 1, we tabulate the measured interband transition energies (E_{ii}^{exp}) and d_{AFM} obtained for 10 different SWNTs. We also show calculated interband transition energies^{25,26} (E_{ii}^{calc}) and the true tube diameters (d_{NT}) for SWNTs having values that are closest to our experimental values. By plotting d_{AFM} versus d_{NT} for all 10 SWNTs (inset, Figure 2c), we obtain a linear relation with an offset of 0.2 nm (best fit: $d_{\text{NT}} = 1.0 d_{\text{AFM}} + 0.2$ nm). On the basis of this result, we use a corrected experimental diameter $d_{\text{exp}} = d_{\text{AFM}} + 0.2$ nm to estimate the actual tube diameter d_{NT} , and this offset effectively accounts for the assorted van der Waals interactions during AFM measurement. Our Rayleigh spectra and calibrated AFM heights allows us to construct an experimental Kataura plot²⁶ from individual tube measurements as shown in Figure 2c. We successfully assigned specific interband transitions for 80 pristine SWNTs, denoted by E_{ii}^S for semiconducting and

E_{ii}^M for metallic SWNTs. Our experimental data show good agreement with previously established values determined by ensemble measurements^{27–29} and those predicted by an empirical tight binding model.^{25,26} Within our excitation range, most SWNTs with d_{exp} above 1.5 nm exhibit two peaks (E_{35}^S, E_{44}^S) in their Rayleigh spectra and are semiconducting. Tubes that lie along the E_{32}^S and E_{11}^M lines generally show a single peak, even though some metallic tubes exhibit two peaks (as shown in Table 1) due to trigonal warping.²⁵ Thus, combining spectral information and calibrated AFM measurements confirms that the optical spectra shown in Figure 2a,b correspond to E_{11}^M and E_{35}^S/E_{44}^S transitions for metallic and semiconducting SWNTs, respectively, along with the chiral indices for the nanotubes shown in Figure 2b and Table 1.

Our electronic-type and (n, m) assignments for SWNTs were confirmed using resonant micro-Raman spectroscopy (RRS). We first used Rayleigh spectroscopy to identify SWNTs with resonances near the wavelength of the Raman excitation laser, 633 nm. The 2D Raman image (Figure 2e) generated from the intensity of the G-band spectral region shows good spatial correspondence with the Rayleigh image of the same area taken at 633 nm (Figure 2d). Tubes were determined to be semiconducting (Figure 2f) or metallic (Figure 2g) based on the lineshapes of the G-band in their Raman spectra (Lorentzian vs Breit–Wigner–Fano lineshapes, respectively),²¹ and these assignments were consistent with our Rayleigh/AFM-based assignments for all SWNTs for which such comparisons were made (denoted by open markers in Figure 2c).¹⁷ Furthermore, we applied all three measurements (Rayleigh, AFM, and RRS) on one nanotube (denoted by green stars in Figure 2c,f) to compare the results. This nanotube has two peaks in its Rayleigh spectrum centered at 1.87 and 2.56 eV with its AFM height measured to be $d_{\text{AFM}} = 1.51$ nm ($d_{\text{exp}} = 1.71$ nm). The structural assignment^{17,7} was made to this nanotube with $d_{\text{NT}} = 1.72$ nm, which makes it a semiconducting nanotube. The Lorentzian line shape of its Raman G-band (Figure 2f) indeed confirms its semiconducting behavior, and the frequency of its radial breathing mode $\omega_{\text{RBM}} = 144$ cm^{-1} (inset, Figure 2f) corresponds to a SWNT diameter $d_{\text{RBM}} = 1.72$ nm (estimated from $d_{\text{RBM}} = 248$ $\text{cm}^{-1}/\omega_{\text{RBM}}$),²¹ thus confirming the chiral index assignment made based on our technique.

A second application of the on-chip Rayleigh imaging is to identify and locate sudden changes in the optical spectra along the length of individual carbon nanotubes. While most SWNTs exhibit uniform Rayleigh spectra throughout their entire length as in Figure 1e, we also observe some nanotubes that exhibit abrupt changes in their spectra as well. The Rayleigh image in Figure 3a contains a nanotube that exhibits a noticeable color change along its length in the region outlined in red. We show the Rayleigh spectrum of the junction along the SWNT axis in Figure 3b together with its matching color image in Figure 3c. The spectral change occurs abruptly, and the corresponding AFM data (Figure 3d)

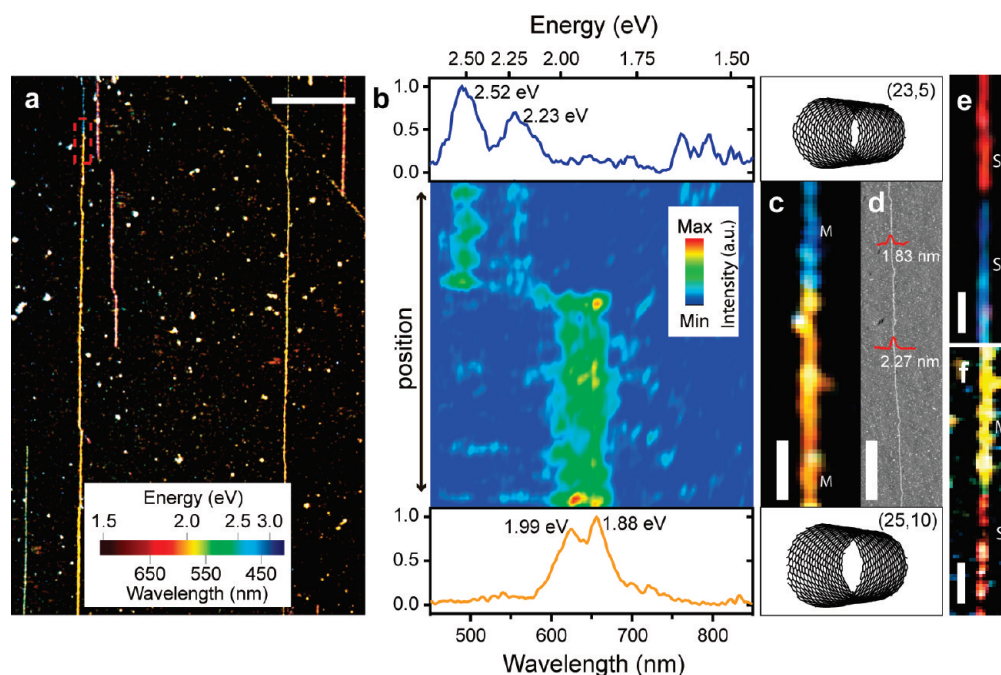


FIGURE 3. SWNT heterojunctions. (a) Large spatial map of SWNT resonances in false color corresponding to λ_{peak} . In the region outlined in red, a SWNT exhibits a distinct color change. Scale bar, $20\ \mu\text{m}$. (b) Rayleigh spectrum along the SWNT axis for the region outlined in red in (a). The observed resonances correspond to E_{22}^{M} transitions for (23, 5) and (25, 10) SWNTs. (c,d) Close-up color image (c) of the outlined region in (a) and corresponding AFM image (d). Scale bars, $2\ \mu\text{m}$. (e,f) Examples of semiconductor–semiconductor (e) and metal–semiconductor (f) heterojunctions. Scale bars, $2\ \mu\text{m}$.

shows that d_{AFM} is slightly different before and after the junction. Optical and AFM measurements imply that this tube forms a metal–metal junction from (23, 5) and (25, 10) nanotubes with the optical resonances corresponding to E_{22}^{M} transitions. (The observed splitting in their Rayleigh spectra is attributed to trigonal warping.) We observed S–M and S–S heterojunctions (Figure 3e,f) as well. Although Rayleigh measurements were used to identify similar chirality-changing events previously,³⁰ the current technique enables us to determine the precise position of such events along with the AFM heights before and after the transition. We find that all chirality-changing events are spatially abrupt, and the transition of the Rayleigh spectra occurs within the length of one pixel of our CCD camera, which corresponds to approximately $150\ \text{nm}$ (Figure 3b,c). We can identify almost all such events that occur among the many SWNTs that we analyzed on our sample. On the basis of our measurements of more than 200 SWNTs, we conclude that the frequency of chirality-changing events for this particular growth procedure is approximately 3% (corresponding to a probability of approximately 1 defect per millimeter of tube length). This technique should be useful for correlating the density of chirality-changing defects in SWNTs produced using different growth conditions.

As a third application of on-chip Rayleigh imaging, we quantitatively studied the effect of intertube interactions on the optical response of a pair of SWNTs with varying separation distances. Figure 4a shows an AFM image of two SWNTs (α and β) that meet and run parallel to one another over a

distance of $3\ \mu\text{m}$ while separated by an average distance of $75\ \text{nm}$, and eventually form a bundle (illustrated in Figure 4b). When separated from one another, SWNTs α and β have Rayleigh scattering peaks at $1.67\ \text{eV}$ (corresponding to E_{11}^{M} transition) and $2.33\ \text{eV}$ (E_{22}^{M}), respectively, as shown in the top panel of Figure 4c. While running parallel and separated by approximately $75\ \text{nm}$, SWNTs α and β exhibit slight blue and red shifts in their Rayleigh scattering spectra, respectively, along with an increase in the peak scattering intensity. Upon bundling, the Rayleigh peaks of SWNTs α and β are even more blue and red shifted, and the peak scattering intensities of the nanotubes when bundled are more than double compared to those of the isolated SWNTs. (See Supporting Information for more quantitative plots of the data in Figure 4 as well as additional Rayleigh measurements on other SWNT bundles.) The effects of intertube coupling and the associated spectral changes were previously measured using Rayleigh⁵ and Raman spectroscopy,² and were attributed to an electromagnetic screening effect rather than direct quantum mechanical tunneling. Indeed, our observation of long-range intertube coupling effects for unbundled nanotubes provides strong experimental evidence against quantum tunneling effects, since these are negligible for such a large intertube distance. Furthermore, the observed blue shifts for the spectral peak for SWNT α suggests that the mechanism for intertube coupling might be influenced by factors other than dielectric screening (which generally causes red shifts). Instead, both the direction and the magnitude of the energy shift in a coupled

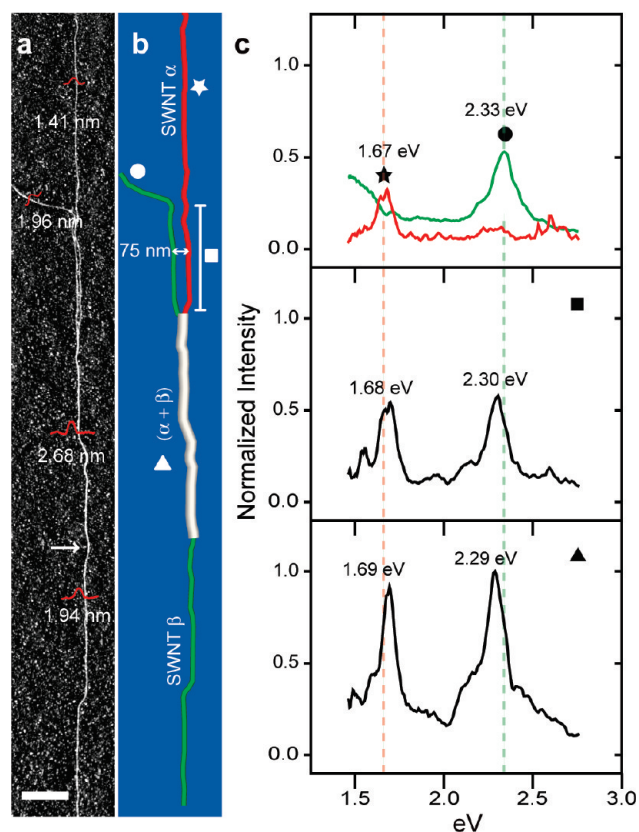


FIGURE 4. Intertube coupling. (a,b) AFM image (a) and corresponding schematic (b) of initially isolated SWNTs α and β meeting and running parallel then finally forming a bundle (bundling region indicated by $(\alpha + \beta)$), with the white arrow indicating the terminal end of SWNT α . Scale bar, 1 μm . c, Normalized Rayleigh scattering spectra with symbols corresponding to different locations in the schematic in (b). Dashed reference lines show that as the distance between the nanotubes decreases, the Rayleigh scattering peak for SWNT β red shifts, while that of SWNT α blue shifts.

nanotube may vary depending on not only the spatial distance but also the resonance energy and spectral peak width of the other nanotube. Both theoretical and experimental investigation is under way in order to understand this behavior.

The on-chip Rayleigh imaging method presented here provides a powerful characterization technique for individual carbon nanotubes, offering rapid feedback of key nanotube properties to specific growth conditions. This should accelerate the optimization of synthesis and purification efforts for producing carbon nanotubes of specific chiralities. The method can also be used to monitor chemical modifications to carbon nanotubes with minimal changes to the experimental setup. We expect our technique will allow novel optical studies of functional optical materials with detailed spatial and spectral resolution, paving a route for engineering and optimization of a variety of nanoscale optoelectronic devices, including photovoltaic devices.

Acknowledgment. We thank P. L. McEuen for useful discussions. The authors also thank Y. J. Kim for assistance

with sample fabrication. This work was supported by the NSF through the Center for Nanoscale Systems, Cornell Center for Materials Research, Center for Chemical Innovation, and NSF CAREER grant. Additional funding was received from the DoD through AFOSR DURIP. Sample fabrication was performed at the Cornell Nanoscale Science and Technology Facility, a National Nanotechnology Infrastructure Network node.

Supporting Information Available. Sample preparation for Rayleigh imaging, AFM measurements, confirmation of Rayleigh scattering signal, Rayleigh imaging-AFM correspondence, diameter distribution of SWNTs, optical response of SWNTs versus MWNTs, shifts in Rayleigh peak position and intensity in SWNT bundles, an additional SWNT bundling example, and details of confocal Raman setup are provided. This material is available free of charge via the Internet at <http://pubs.acs.org>.

REFERENCES AND NOTES

- Choi, J. H.; Strano, M. S. *Appl. Phys. Lett.* **2007**, *90* (22), 223114.
- Fantini, C.; Jorio, A.; Souza, M.; Strano, M. S.; Dresselhaus, M. S.; Pimenta, M. A. *Phys. Rev. Lett.* **2004**, *93* (14), 147406.
- Wang, F.; Sfeir, M. Y.; Huang, L.; Huang, X. M. H.; Wu, Y.; Kim, J.; Hone, J.; O'Brien, S.; Brus, L. E.; Heinz, T. F. *Phys. Rev. Lett.* **2006**, *96* (16), 167401.
- O'Connell, M. J.; Sivaram, S.; Doorn, S. K. *Phys. Rev. B* **2004**, *69* (23), 235415.
- Fuhrer, M. S.; Nygard, J.; Shih, L.; Forero, M.; Yoon, Y. G.; Mazzone, M. S. C.; Choi, H. J.; Ihm, J.; Louie, S. G.; Zettl, A.; McEuen, P. L. *Science* **2000**, *288* (5465), 494–497.
- Collins, P. G.; Bradley, K.; Ishigami, M.; Zettl, A. *Science* **2000**, *287* (5459), 1801–1804.
- Zuo, J. M.; Vartanyants, I.; Gao, M.; Zhang, R.; Nagahara, L. A. *Science* **2003**, *300* (5624), 1419–1421.
- Odom, T. W.; Huang, J. L.; Kim, P.; Lieber, C. M. *Nature* **1998**, *391* (6662), 62–64.
- Wildoer, J. W. G.; Venema, L. C.; Rinzler, A. G.; Smalley, R. E.; Dekker, C. *Nature* **1998**, *391* (6662), 59–62.
- Lin, H.; Lagoute, J.; Repain, V.; Chacon, C.; Girard, Y.; Lauret, J. S.; Ducastelle, F.; Loiseau, A.; Rousset, S. *Nat. Mater.* **2010**, *9* (3), 235–238.
- Wang, F.; Dukovic, G.; Brus, L. E.; Heinz, T. F. *Science* **2005**, *308* (5723), 838–841.
- Sfeir, M.; Beetz, T.; Wang, F.; Huang, L.; Huang, X.; Huang, M.; Hone, J.; O'Brien, S.; Misewich, J.; Heinz, T.; Wu, L.; Zhu, Y.; Brus, L. *Science* **2006**, *312* (5773), 554–556.
- Sfeir, M.; Wang, F.; Huang, L.; Chuang, C.; Hone, J.; O'Brien, S.; Heinz, T.; Brus, L. *Science* **2004**, *306* (5701), 1540–1543.
- Bachilo, S.; Strano, M.; Kittrell, C.; Hauge, R.; Smalley, R.; Weisman, R. *Science* **2002**, *298* (5602), 2361–2366.
- O'Connell, M. J.; Bachilo, S. M.; Huffman, C. B.; Moore, V. C.; Strano, M. S.; Haroz, E. H.; Rialon, K. L.; Boul, P. J.; Noon, W. H.; Kittrell, C.; Ma, J. P.; Hauge, R. H.; Weisman, R. B.; Smalley, R. E. *Science* **2002**, *297* (5581), 593–596.
- Berciaud, S.; Cognet, L.; Poulin, P.; Weisman, R. B.; Lounis, B. *Nano Lett.* **2007**, *7* (5), 1203–1207.
- Kukovecz, A.; Kramberger, C.; Georgakilas, V.; Prato, M.; Kuzmany, H. *Eur. Phys. J. B* **2002**, *28* (2), 223–230.
- Jorio, A.; Saito, R.; Hafner, J.; Lieber, C.; Hunter, M.; McClure, T.; Dresselhaus, G.; Dresselhaus, M. *Phys. Rev. Lett.* **2001**, *86* (6), 1118–1121.
- Saito, R.; Dresselhaus, G.; Dresselhaus, M. S., *Physical Properties of Carbon Nanotubes*; Imperial College Press: London, 1998.
- Ando, T. *J. Phys. Soc. Jpn.* **1997**, *66* (4), 1066–1073.
- Dresselhaus, M.; Dresselhaus, G.; Saito, R.; Jorio, A. *Phys. Rep.* **2005**, *409* (2), 47–99.

- (22) Berciaud, S.; Voisin, C.; Yan, H. G.; Chandra, B.; Caldwell, R.; Shan, Y. Y.; Brus, L. E.; Hone, J.; Heinz, T. F. *Phys. Rev. B* **2010**, *81* (4), No. 041414.
- (23) Berciaud, S.; Cognet, L.; Lounis, B. *Phys. Rev. Lett.* **2008**, *101* (7), 077402.
- (24) Kocabas, C.; Hur, S. H.; Gaur, A.; Meitl, M. A.; Shim, M.; Rogers, J. A. *Small* **2005**, *1* (11), 1110–1116.
- (25) Saito, R.; Dresselhaus, G.; Dresselhaus, M. S. *Phys. Rev. B* **2000**, *61* (4), 2981–2990.
- (26) Kataura, H.; Kumazawa, Y.; Maniwa, Y.; Umez, I.; Suzuki, S.; Ohtsuka, Y.; Achiba, Y. *Synth. Met.* **1999**, *103* (1–3), 2555–2558.
- (27) Strano, M. J. *Am. Chem. Soc.* **2003**, *125* (51), 16148–16153.
- (28) Weisman, R. B.; Bachilo, S. M. *Nano Lett.* **2003**, *3* (9), 1235–1238.
- (29) Strano, M.; Doorn, S.; Haroz, E.; Kittrell, C.; Hauge, R.; Smalley, R. *Nano Lett.* **2003**, *3* (8), 1091–1096.
- (30) Chandra, B.; Bhattacharjee, J.; Purewal, M.; Son, Y. W.; Wu, Y.; Huang, M. Y.; Yan, H. G.; Heinz, T. F.; Kim, P.; Neaton, J. B.; Hone, J. *Nano Lett.* **2009**, *9* (4), 1544–1548.

Supporting Online Information for

On-Chip Rayleigh Imaging and Spectroscopy of
Carbon Nanotubes

*Daniel Y. Joh^{1,2}, Lihong H. Herman¹, Sang-Yong Ju², Jesse Kinder², Michael A. Segal²,
Jeffreys N. Johnson², Garnet K. L. Chan², and Jiwoong Park^{2,3,†}*

¹School of Applied and Engineering Physics, Cornell University, Ithaca, NY, 14853 USA

²Department of Chemistry and Chemical Biology, Cornell University, Ithaca, NY, 14853
USA

³Kavli Institute at Cornell for Nanoscale Science, Cornell University, Ithaca, NY, 14853
USA

[†]To whom correspondence should be addressed. Email: jpark@cornell.edu

Supplementary Information Contents

1. Device Fabrication
2. Sample Preparation for Rayleigh Imaging
3. Atomic Force Microscopy
4. Experimental Apparatus for On-Chip Rayleigh Imaging
Figure S1: Schematic of on-chip Rayleigh imaging setup
5. Confirmation of Rayleigh Scattering Signal
Figure S2: CCD Images with and without matching bandpass filters
6. Normalization and Construction of Rayleigh Images and Spectra
Figure S3: Wavelength-dependence of excitation and detection elements
7. Rayleigh Imaging-AFM Correspondence
Figure S4: Correspondence between Rayleigh and AFM Imaging
8. Diameter Distribution of SWNTs
Figure S5: Diameter Distribution of typical SWNT sample
9. Optical Response of Multi-Walled vs. Single-Walled Carbon Nanotubes
Figure S6: SWNT Optical Response vs. that of MWNTs
10. Shifts in Rayleigh Peak Position and Intensity in SWNT Bundles (Main text Fig. 4a-c)
Figure S7: Energy shift and Intensity vs. Gap Distance
11. Additional SWNT Bundling Example
Figure S8: SWNT Bundling
12. Confocal Raman Setup
Figure S9: Schematic of Raman setup

1. Device Fabrication

All fabrication was performed using conventional photolithography on commercially available ST-cut quartz wafers (Hoffman Materials, LLC). A reactive-ion etching system was used to etch alignment marks 400 nm deep. The wafers were diced and substrates were placed in a quartz reaction tube and annealed in air at 900°C for 9 hours. The catalyst pattern was then defined by photolithography, and 2 Å of Fe was evaporated onto individual substrates. Following lift off, aligned SWNTs were grown using a procedure adapted from Kocabas *et al.* (*Small* **1**, 1110 (2005)) at 865°C using methane as the carbon feedstock.

2. Sample Preparation for Rayleigh imaging

First, cover glasses (Corning, No.1, 22 mm squares) were rigorously cleaned by placing them in a 3:1 mixture of H₂SO₄: H₂O₂ at 90°C for 30 min and subsequently rinsing them with deionized water and isopropyl alcohol, followed by drying under a flow of N₂. Next, the SWNT substrate was placed in a quartz reaction tube and annealed at 275°C under a constant flow of H₂ (350 sccm) and Ar (500 sccm) for 10 minutes. Finally, a drop of glycerol (Sigma-Aldrich, ≥ 99.5 % spectrophotometric grade) preheated to 100°C was applied between the SWNT substrate and coverglass and held together by Scotch tape.

3. Atomic Force Microscopy

To make optical vs. AFM comparisons (such as those shown in Fig. S4), we first located SWNTs on the sample using our optical setup. Using the pre-patterned alignment

marks on the substrates as guides, we subsequently obtained AFM images and diameters after taking extra care to remove the glycerol from the sample (since residual glycerol can significantly affect the AFM measurement). To remove the glycerol, the sample was first soaked for a full day in ethanol, and then thoroughly rinsed with deionized water, acetone, and finally isopropanol. After drying the substrate with N₂, the sample was placed in a quartz tube and annealed at 300° C for at least 15 minutes under a constant flow of H₂ (300 sccm) and Ar (500 sccm) to eliminate any residual glycerol or solvents. The sample was then taken to the AFM for imaging and height analysis.

AFM imaging was performed in air using a commercial MFP3D AFM (Asylum Research, Santa Barbara, CA) in tapping mode with free oscillating amplitude of 71 nm and set point of 52 nm for all measurements. Diameter measurements were performed in repulsive mode ($\phi < 90^\circ$) with a scanning rate of 1Hz and scan size of $\sim 1\mu\text{m}$. 300 kHz aluminum-coated SiO₂ cantilevers (Budget Sensors, Bulgaria) were purchased from Ted Pella Inc. SWNT diameter was determined by fitting AFM height traces to a Gaussian function and averaging the fitted amplitudes of several measurements (> 3)

4. Experimental Apparatus for On-Chip Rayleigh Imaging

Detailed schematic of the experimental apparatus is shown in Fig. S1. The quartz substrate containing aligned SWNTs was coated with glycerol, whose refractive index is similar to that of quartz. The broadband excitation laser (L) is linearly polarized (P) and the wavelength and bandwidth are controlled by a monochromator (M). The excitation laser is introduced into the sample at an angle using a darkfield condenser (DCW) and reflected completely at the uppermost quartz-air interface by total internal reflection,

preventing the exciting laser from entering the detection optics. The total laser power at the sample varies between 0.1 mW and 1 mW (depending on the wavelength) using a typical bandwidth of 20 nm. The scattered light is collected by a high numerical aperture objective lens (OL) (N.A. = 0.95) and focused onto a 2D array detector (CCD) (Sensicam QE, Cooke Corporation) via tube lens (TL).

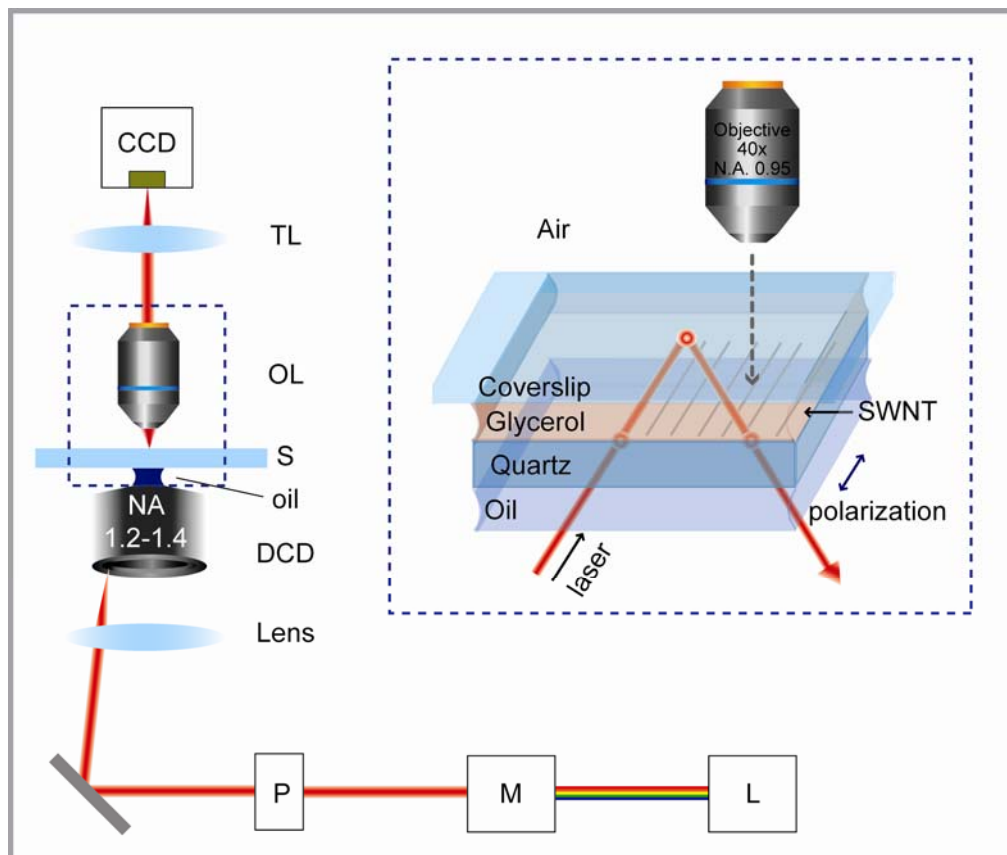


Figure S1. Schematic of on-chip Rayleigh imaging setup. See text above for abbreviations.

5. Confirmation of Rayleigh Scattering Signal

Using the geometry described in Fig. S1, images were taken using a CCD camera with and without a bandpass filter (bandwidth < 10 nm) in the detection pathway

matching the excitation wavelength (bandwidth < 5nm) with exposure time of 7 seconds (see Fig. S2). These images confirm that the majority of the collected photons are due to the elastic scattering of SWNTs, as opposed to Raman scattering or photoluminescence. The scattering intensity with and without a bandpass filter (I_F and I_o , respectively) were measured, and their ratio was typically $I_F/I_o \approx 0.61$, similar to the transmission of the bandpass filter.

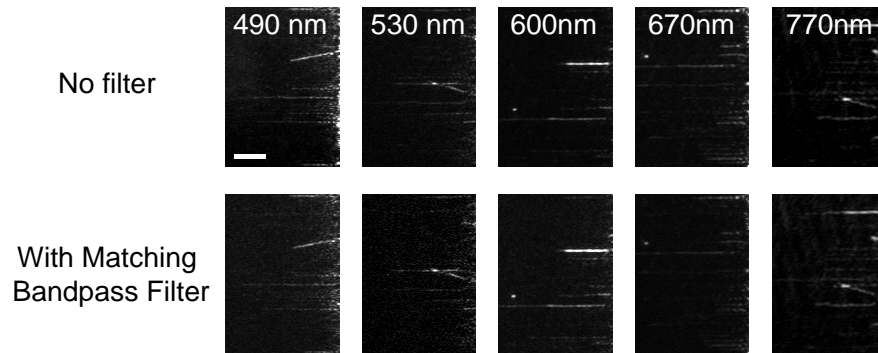


Fig. S2: CCD Images with and without matching bandpass filters. Black and white images taken with and without a bandpass filter (bandwidth < 10 nm) matching the excitation wavelength in the detection pathway. Scale bar, 5 μm

6. Normalization and Construction of Rayleigh Images and Spectra

Below we show plots for the quantum efficiency of the CCD camera (Fig. S3a) and for the wavelength-dependence of the excitation laser power before it hits the sample (i.e. after monochromator and additional optical elements) (Fig. S3b). For the wavelength range of our experiment, the traces of both graphs do not change very rapidly. As a result, within our experimental peak width (~ 100 meV), we can assume very slow change, and thus the wavelength-dependence of the detection efficiency and excitation profile will not affect the lineshapes of the SWNT resonance significantly.

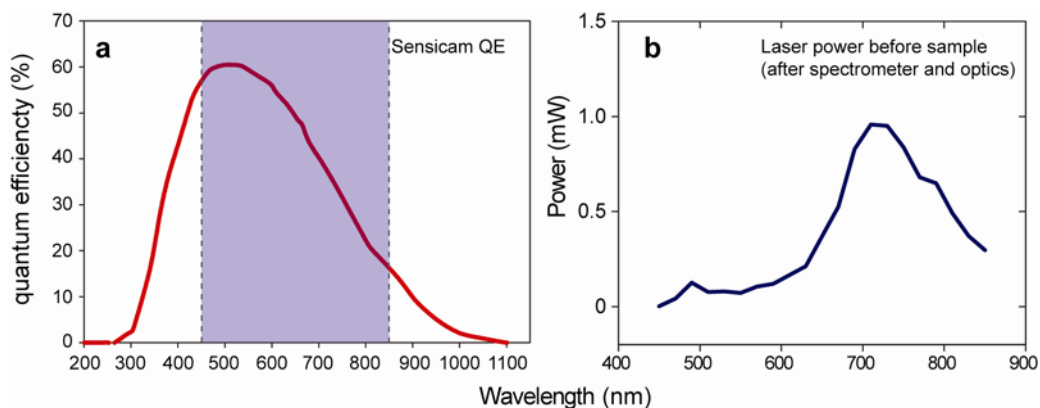


Figure S3: Wavelength-dependence of excitation and detection elements.

Quantum efficiency of the CCD camera (**a**) and profile of the excitation laser before hitting the sample (**b**) as a function of wavelength. The wavelength range used in this experiment is highlighted in blue.

The Rayleigh images and spectra for SWNTs are constructed using a frame-by-frame calibration protocol. The dark current count was first subtracted from each frame. To correct for the background due to out-of-plane scattering and autofluorescence of the medium, we applied a background subtraction/low-pass spatial filter using the image processing software ImageJ (Rasband, W.S., ImageJ, U. S. National Institutes of Health). Next, to calibrate for the detection efficiency of the detector and changes in the excitation laser all as a function of wavelength, each frame was divided by the spatial profile of the illumination fitted to a 2D Gaussian. This resulted in each frame (which corresponds to a particular wavelength) being calibrated for wavelength-dependent fluctuations in the camera and excitation laser while normalizing the overall intensity for each frame.

Since each frame (out of the total 200) represents a 2 nm step, each pixel comprising the composite spatial image (also commonly known as an “image stack”) of

the illuminated area (approximately $70 \times 80 \mu\text{m}^2$) corresponds to a spectral profile. To extract spectral profiles for SWNTs, we traced the integrated light intensity per unit length measured from the pixels in the image stack in which SWNTs appeared using ImageJ.

7. Rayleigh Imaging-AFM Correspondence

We compared our optical images to their corresponding AFM images in order to confirm that SWNTs on the substrate were visible under our Rayleigh imaging scheme. Fig. S4 shows a representative colour Rayleigh images compared to an AFM images of the same area.

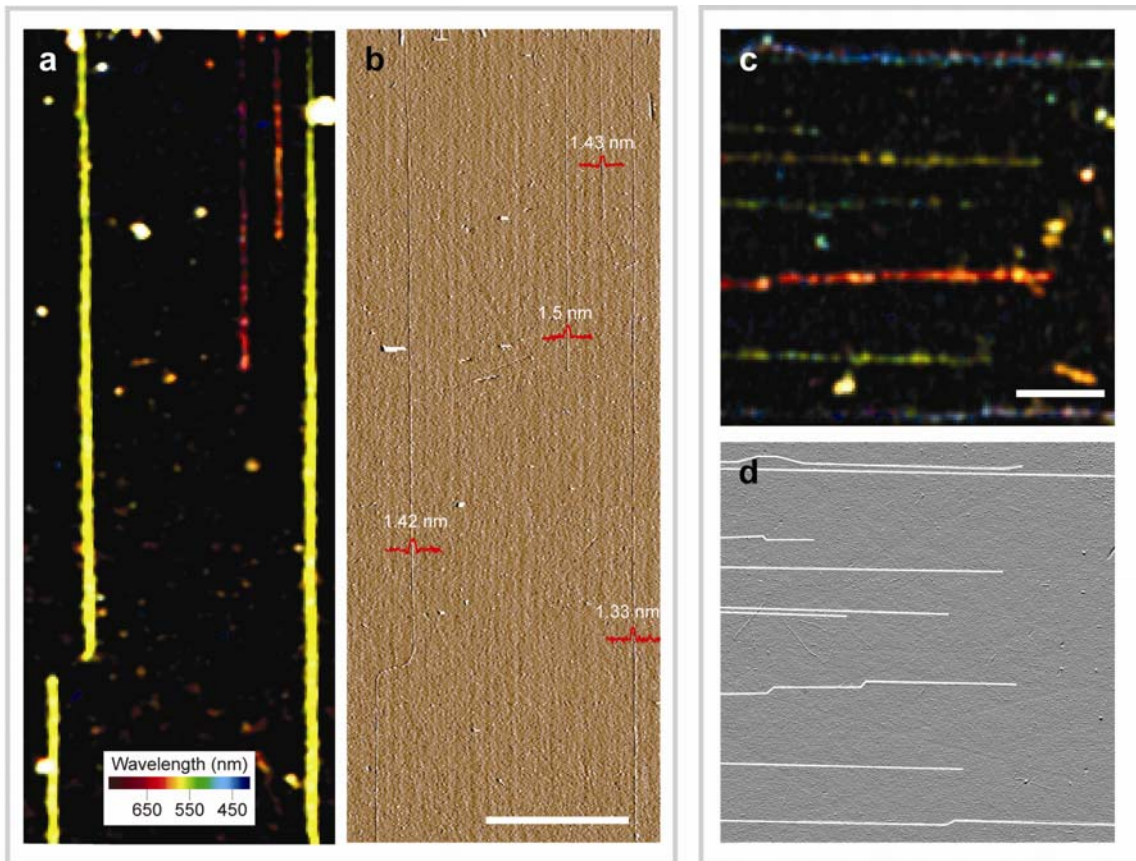


Figure S4. Correspondence between Rayleigh and AFM Imaging. **a, b**, Color Rayleigh image (**a**) and matching AFM image (**b**). Scale bar, 10 μm . **c, d**, Color Rayleigh image (**c**) and matching AFM image (**d**) for a different region. For the AFM image in (**d**), the SWNTs are outlined in white for clarity. Scale bar, 5 μm .

8. Diameter Distribution of SWNTs

Fig. S5 shows the diameter distributions we measured for the SWNTs studied in our sample. The distribution in (**a**) is centred at 1.2 ± 0.5 nm, ranging from 0.5 nm to 2.2 nm.

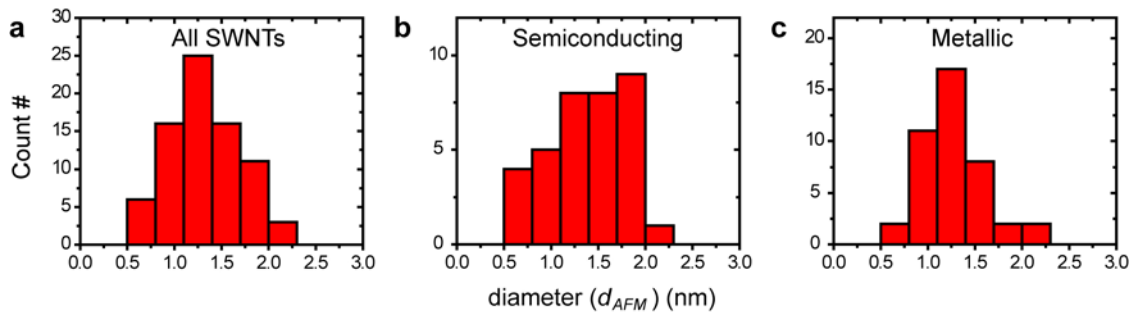


Figure S5. Diameter Distribution of typical SWNT sample. **a, b, c**, Diameter distribution (d_{AFM}) for all SWNTs studied (**a**), semiconducting SWNTs (**b**), and metallic SWNTs (**c**).

9. Optical Response of Multi-Walled vs. Single-Walled Carbon Nanotubes

SWNTs can easily be distinguished from MWNTs from their distinct optical spectra. For instance, the MWNT shown in the Rayleigh image in Fig. S6a has a broad optical

response (as shown by its Rayleigh spectrum in Fig. S6c), whereas the SWNT exhibits a single sharp peak in its Rayleigh scattering spectrum (Fig. S6b).

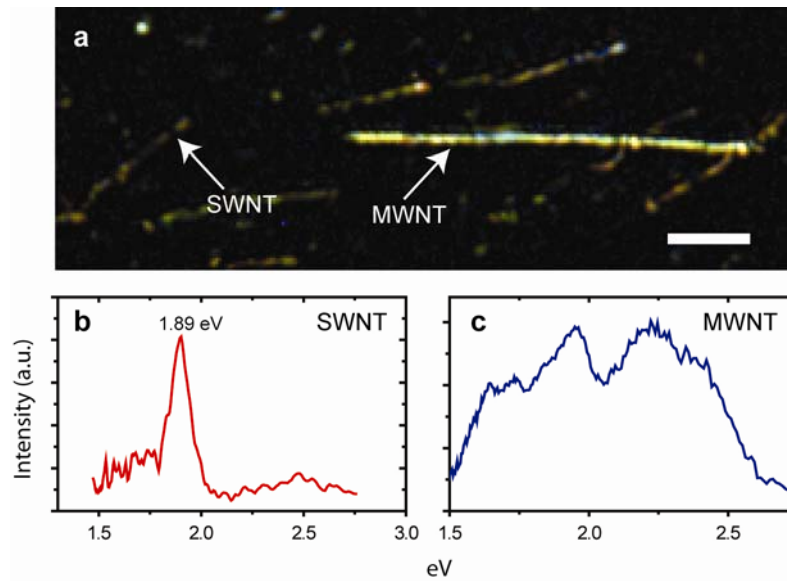


Figure S6. SWNT Optical Response versus that of MWNTs. a, Color Rayleigh image of randomly dispersed nanotube growth. Arrows indicate a SWNT and MWNT. **b, c,** Corresponding Rayleigh spectra of the SWNT (**b**) and MWNT (**c**)

10. Shifts in Rayleigh Peak Position and Intensity in SWNT Bundles (Main Text Fig. 4a-c)

Shown in Fig. 4 of the main text is a pair of nanotubes that are initially isolated, then run parallel with a separation distance of 75 nm, and finally become bundled. Fig. S7a illustrates this configuration. Fig. S7b plots the shift in peak position (denoted by ΔE) for SWNTs α and β as a function of gap distance for the regions marked by the symbols, and Fig. S7c plots the normalized intensity as a function of gap distance between the tubes.

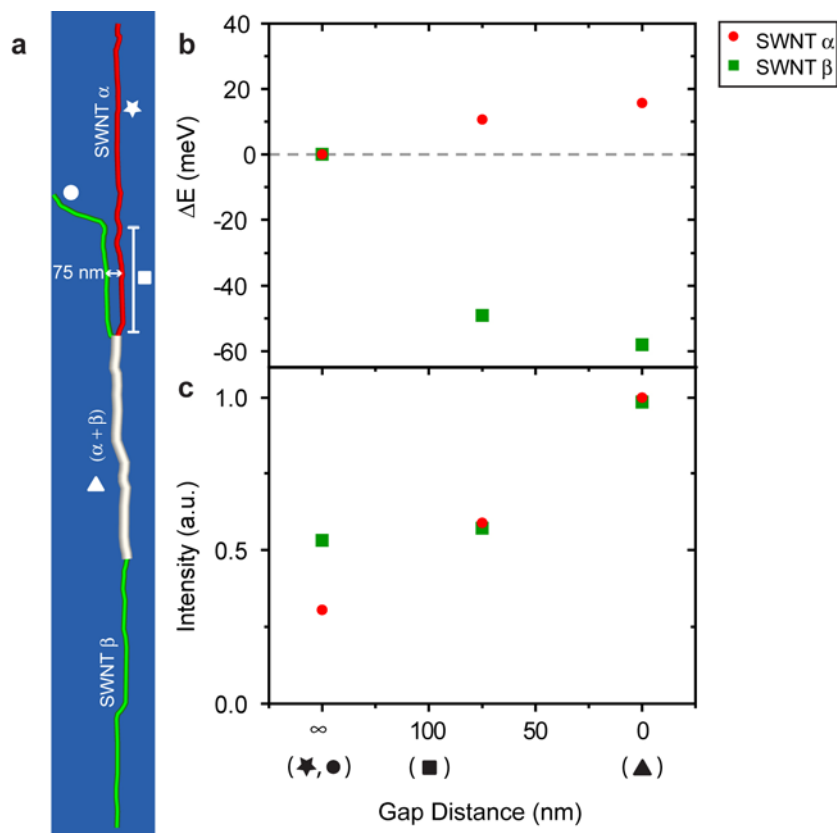


Figure S7. Energy Shift and Intensity vs. Gap Distance. **a**, Illustration depicting the bundling configuration for SWNTs α and β . **b**, Shift in Rayleigh scattering peak position (ΔE) versus gap distance between the tubes. **c**, Normalized Rayleigh scattering intensity versus gap distance between the tubes.

11. Additional SWNT Bundling Example

We were furthermore able to probe the effects of intertube coupling for nanotubes in a slightly different geometry than that shown in Fig. 4. Fig. S8a shows the Rayleigh image of two SWNTs (δ and γ) forming a bundle in the region indicated by the dashed red lines (close-up AFM image of the bundling junction shown in the inset of Fig. S8b). The nanotubes remain bundled in the region marked by $(\delta + \gamma)$ and eventually SWNT γ

stops abruptly at the location marked by the white arrow. The peak scattering intensity of SWNT δ in its bundled state is significantly larger compared to when it is isolated. The point at which SWNT δ is no longer bundled was determined by examining the intensity of the Rayleigh scattering signal along the nanotube axis. In addition, we observe that the spectral peak for SWNT δ is redshifted by about 10 meV when it is in the bundled state. The increase in scattering intensity and magnitude of the redshift in the Rayleigh scattering peak are consistent with Rayleigh scattering measurements performed in air on bundled nanotubes suspended across lithographically defined slits (*Phys. Rev. Lett.* **96**, 167401).

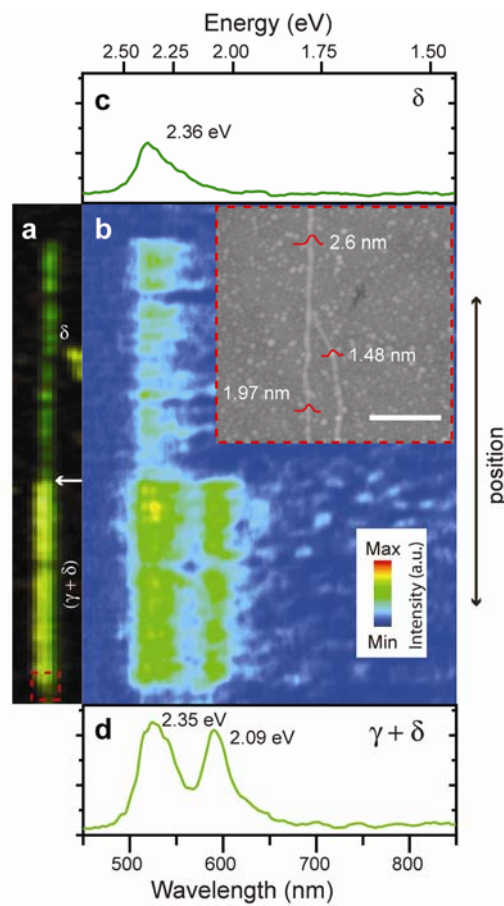


Figure S8. SWNT Bundling. **a**, Rayleigh image of a nanotube bundle comprised of SWNTs δ and γ . The tubes are bundled in the region marked by $(\delta + \gamma)$ until the

location marked by the white arrow, at which point SWNT δ outgrows SWNT γ . Scale bar, 5 μm . **b**, Contour plot of the optical response as a function of excitation wavelength along nanotube axis. Inset: Enlarged AFM image of the bundling junction, denoted in the Rayleigh image (**a**) by the dashed red box. Scale bar, 500 nm. **c**, **d**, Normalized Rayleigh scattering spectra for isolated SWNT δ (**c**) and bundled SWNTS ($\delta + \gamma$) (**d**).

12. Confocal Raman Setup

Raman spectra were obtained using a custom-built confocal Raman setup using an inverted microscope (Olympus IX71) as the main platform. The excitation diode laser centered at 632.8 nm. Scattered Raman signals were collected using a backscattering geometry as shown in Figure S6. Collected signals were analyzed using gratings of either 300g/mm or 1200g/mm for spatial 2D and point imaging, respectively. The spectral wavelength was calibrated using a Si substrate as an external reference.

Details of Raman setup: The Raman setup was built on a vibration-isolated optical table in a room isolated from external light. The schematic in Figure S6 illustrates the experimental apparatus for confocal Raman spectroscopy. A temperature- and power-controlled diode laser (632.8 nm, $P_{\text{max}} = 35$ mW, Thorlabs) was used as the excitation source. The beam was linearly polarized, collimated, and directed towards the back aperture of a 50 \times objective (UMPlanFL, NA = 0.8, Olympus). The bandwidth of the excitation wavelength is further narrowed via double bandpass filter (632.8 nm, O.D. > 5, bandwidth = 2.4 nm, Semrock). The collimated laser light was focused onto our sample

containing aligned nanotubes. The sample was mounted onto LabVIEW-controlled XYZ stage (scxyz100 piezo stage, Thorlabs). The polarization cube (CM1-PBS1, Thorlabs) and notch filter (632.8 nm, O.D. > 6, bandwidth = 266 cm^{-1} , Kaiser Optical System) were used to reject superfluous scattered light and the majority of the excitation laser, respectively, before Raman signals reached spectrometer (SP2300i, Princeton Instruments), which was connected to the sideport of the microscope. Randomly scattered light was further eliminated by a kinematic slit (ca. 100 μm) and the Raman signal was recorded using a CCD camera (PIXIS 400, Princeton Instruments).

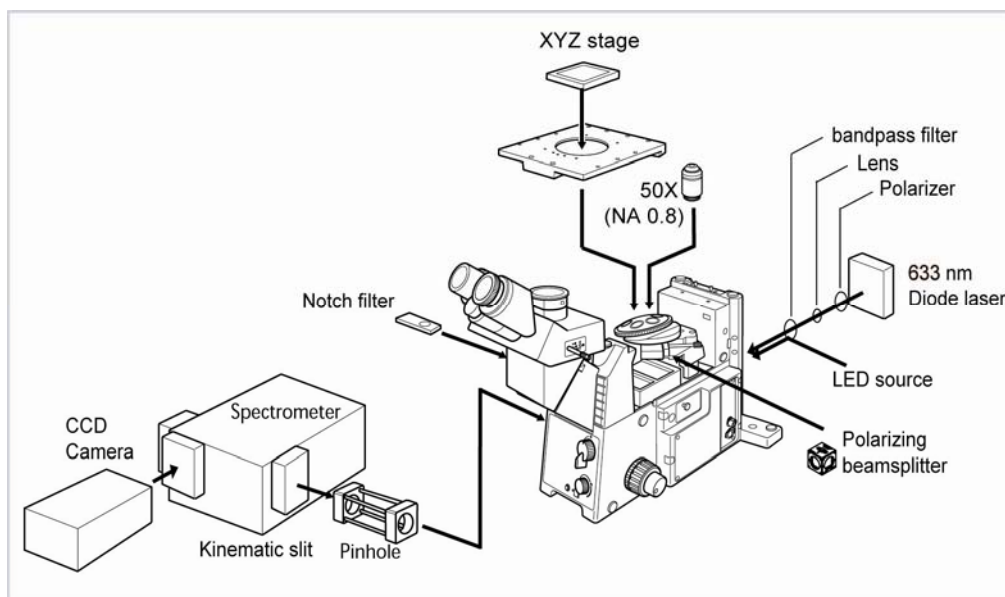


Figure S9. Schematic of Raman setup. Part of the figure was adapted from Olympus IX71 manual.